Enhanced imaging by fusion of illumination series

F. Puente León

Institut für Meß- und Regelungstechnik
Universität Karlsruhe (TH), Postfach 6980
D-76128 Karlsruhe, Germany

ABSTRACT

A novel image processing method is presented that allows to obtain images with maximal constrast by means of fusing a series of images which were acquired under different illumination constellations. For this purpose, the notion of illumination space is introduced, and strategies for sampling this space are discussed. It is shown that the signal of interest contained in a physical texture often would be lost if standard image acquisition methods were used. In contrast to this, the presented approach shows a robust and reproducible way to obtain high-contrast images containing the relevant information for subsequent processing steps.

Keywords: surface image acquisition, illumination, image contrast, illumination series, image fusion

1 INTRODUCTION

Many computer vision tasks are concerned with the analysis of textured surfaces like machined surfaces, firearm bullets or cartridge cases.[1,2,12] For inspection purposes, a stylus gauge can be used to obtain the surface relief. Alternatively, grey-level images can be obtained with a video camera. This latter method does not allow any acquisition of relief data; however, the optical properties of the surface can be utilized to obtain certain features with maximal contrast. A brief comparison of both techniques leads to the conclusion that there are many practical cases in which acquisition of grey-level images is preferable.[13] Since illumination is a critical aspect with respect to image quality and reproducibility of image acquisition conditions, it is desirable to examine the influence of illumination on image quality more closely. However, up to now there have been very few efforts to select or to optimally position lighting devices or even to consider illumination as an active component in computer vision.[16]

2 INFLUENCE OF ILLUMINATION

In the first part of the paper, the influence of illumination on acquisition of images of textured surfaces is investigated. For this purpose it is necessary to have a closer look at the image formation process. There are three factors that mainly determine the grey levels which are obtained from a surface:

- surface orientation and profile,
- incident light pattern, and
- optical properties of the surface.

To allow a better understanding of the image formation process, a synthetic, homogeneously textured surface is defined in section 2.1.[3] Section 2.2 deals with the description of the lighting pattern used for image acquisition. Following, in section 2.3 different models describing the optical properties of the surface will be utilized to examine the influence of illumination on the image intensities by means of simulations. Finally, in section 2.4 conclusions concerning the choice of a suitable illumination strategy will be drawn.

2.1 Definition of a test surface

The effect of illumination is illustrated by means of a test surface. Especially, it has to be analysed how far the contrast of a surface image depends on the illumination direction. Moreover, it is shown how grey-level textures result from surface topography for different illumination constellations. For this purpose, a purely harmonic profile will serve as a test surface:

$$z = f(\bar{x}) := A \cdot \cos x, \qquad \bar{x} = (x, y)^{\mathrm{T}}. \tag{1}$$

This surface has the normal vector:

$$\bar{n} = \frac{1}{\sqrt{1 + A^2 \cdot \sin^2 x}} \begin{pmatrix} A \cdot \sin x \\ 0 \\ 1 \end{pmatrix}, \qquad \|\bar{n}\| = 1. \tag{2}$$

Fig. 1a shows a 3-D plot of the surface for $A = 1$. In Fig. 1b an image of the same surface profile is shown in which the depth data are coded by means of grey levels ($[-1, 1] \rightarrow$ [black,white]). The viewing direction is perpendicular to the x, y-plane.
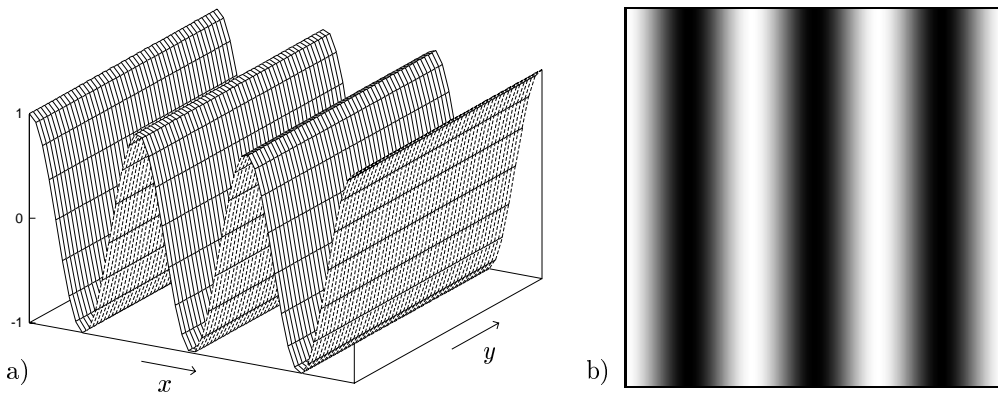

Figure 1. Test surface $z = \cos x$: a) surface profile plot; b) grey-level coded depth data.

2.2 Incident light pattern

For illumination purposes, a distant, collimated point light source is used. Such a light source leads to a spatially constant surface irradiance if a plain surface is assumed. The illumination direction is described by the elevation angle θ_i and the azimuth ϕ_i, which span a two-dimensional *illumination space*. The illumination angle is described by the vector:

$$\bar{\imath} = \begin{pmatrix} \cos \phi_i \cdot \sin \theta_i \\ \sin \phi_i \cdot \sin \theta_i \\ \cos \theta_i \end{pmatrix}. \tag{3}$$

Alternative illumination constellations, e.g. diffuse illumination, may also be considered. However, due to linearity of surface reflectances,[5] the effect of such illumination constellations can be described by superposition of images obtained by means of multiple individual, distant, collimated point light sources. Thus, considering images obtained with different sources, and linear combinations of them, is equivalent.

2.3 Optical properties of the surface

To analyse the influence of illumination in image acquisition, the image formation process has to be examined more closely. The grey levels generated by a camera are quantized measurements of the target irradiance E_p. On the other hand, target irradiance is proportional to the scene radiance L_r.[6] Thus, it is sufficient to consider the scene radiance L_r to examine the effect of illumination on our test surface.

The optical properties of the surface are specified by means of the bidirectional reflectance distribution function (BRDF) $f_\mathrm{r}(\theta_\mathrm{i}, \phi_\mathrm{i}; \theta_\mathrm{r}, \phi_\mathrm{r})$, where θ_r and ϕ_r denote the direction of the reflected radiant flux. The optical properties will be taken into account by utilizing different existing reflection models, namely diffuse, specular, and backscatter reflection. These kinds of reflection can be modelled by superposing three different lobes: Lambertian, forescatter, and backscatter lobe, respectively; see Fig. 2. By combining these reflection models, a sufficiently accurate approximation of the reflection properties of a large class of engineering materials can be achieved.[14]
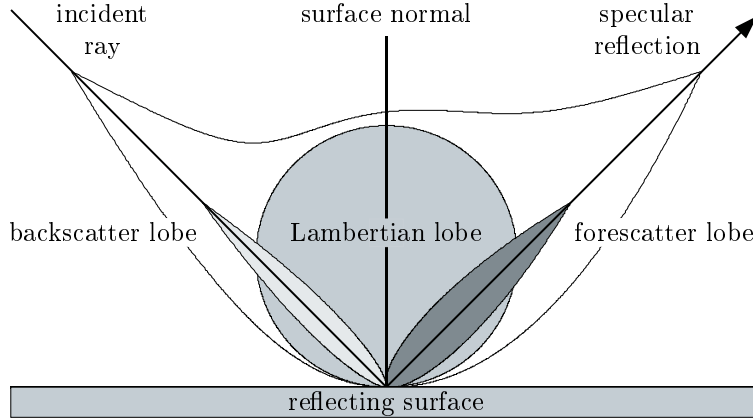
Figure 2. Morphology of reflection from surfaces.

The effect of illumination on image quality will be measured by means of a simple contrast criterion:

$$K := k \cdot \left(\max_{\bar{x}} \left\{ g(\bar{x}) \right\} - \min_{\bar{x}} \left\{ g(\bar{x}) \right\} \right), \tag{4}$$

where k is a normalization factor. This contrast definition is very sensitive in the presence of noise, but since the image data are simulated, this fact is of no account. Of course, other suitable criteria also could have been utilized. However, for the applications presented in section 4, a contrast measure is sufficient.

2.3.1 Diffuse reflection

If we assume a perfectly diffuse reflector (i.e. a Lambertian surface), the surface radiance L_r is proportional to the cosine of the angle between illumination direction $\bar{\imath}$ and surface normal $\bar{n}$:[6]

$$L_\mathrm{r} \propto \max\left(0, \cos\left(\angle(\bar{n}, \bar{\imath})\right)\right) = \max\left(0, \frac{\bar{n} \cdot \bar{\imath}}{|\bar{n}| \cdot |\bar{\imath}|}\right) = \max\left(0, \frac{A \cos\phi_\mathrm{i} \sin\theta_\mathrm{i} \sin x + \cos\theta_\mathrm{i}}{\sqrt{1 + A^2 \sin^2 x}}\right). \tag{5}$$

The imaging configuration for this case is depicted in Fig. 3. The incident light pattern is reflected isotropically, i.e. the surface radiance, and thus the generated image intensities, are independent of the observation angle.

Fig. 5 shows simulated grey-level images of the test surface Fig. (1) illuminated with different light patterns. Images 5a–d were generated by assuming a collimated source for different illumination angles as described in section 2.2. Image 5e was obtained by choosing a purely diffuse illumination pattern. In all cases multiple reflections were neglected, and incoherent, unpolarized light was assumed. Despite of these simplifications, the experiment shows some important qualitative results which should be taken into account when choosing a proper illumination strategy.
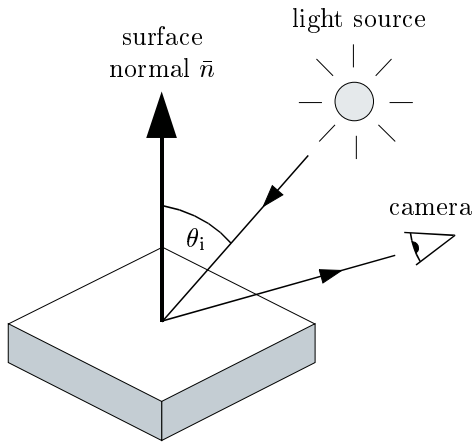
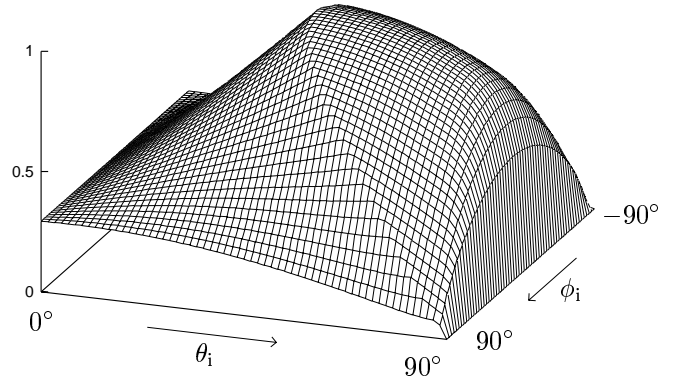**Figure 3.** Diffuse reflection: imaging configuration.

Figure 4. Image contrast of the diffusely reflecting test surface depending on the illumination direction.

a) $\theta_i = 0°$ b) $\theta_i = 22.5°$ c) $\theta_i = 45°$ d) $\theta_i = 67.5°$ e) diffuse illumination
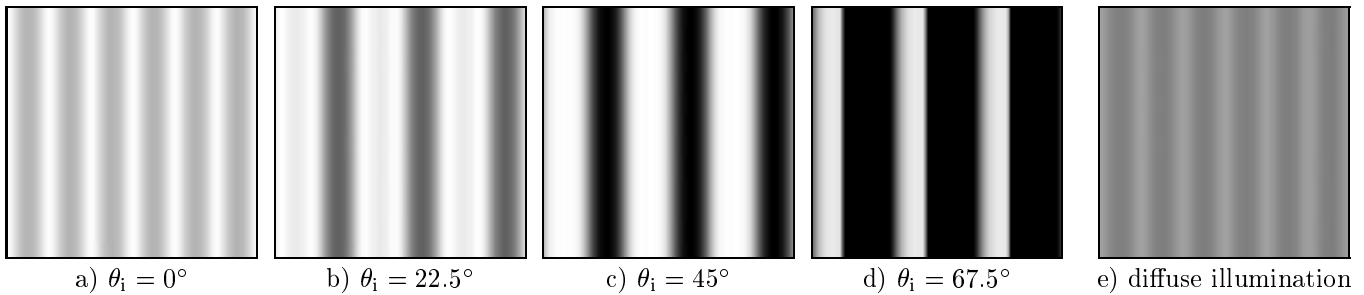
Figure 5. Diffusely reflecting test surface: a–d) parallel illumination ($\phi_i = 0$); e) diffuse illumination.

In Fig. 4 the image contrast K according to eq. (4) is plotted depending on the illumination angles θ_i and ϕ_i of a collimated source. It can be clearly seen that the contrast shows a pronounced maximum when the illumination direction $\bar{\imath}$ is chosen to be perpendicular to the grooves (here: $\phi_i = 0°$), and the elevation angle θ_i is chosen so that appearance of shadows is just avoided. In contrast to this, the diffusely illuminated surface image Fig. 5e shows a much lower contrast than most of the images with parallel lighting. Moreover, an additional undesirable effect of illumination on groove texture imaging can be seen in Fig. 5: particularly, the images a and e suggest that the original texture has double groove density.

2.3.2 Specular reflection

The case of specular reflection is often described by facet models.[14] A rough surface is modeled as being made up of facets, each one being a small perfectly plane reflector, i.e. reflecting incident light specularly. All the facets show a random inclination about the mean surface. In Fig. 6 an example imaging configuration of a surface containing a facet with normal $\bar{c}$ is depicted.

The Torrance-Sparrow model[15] assumes the following distribution of the radiance L_r:

$$L_r(\delta) \propto \exp\left(-\frac{\delta^2}{2\sigma^2}\right), \qquad \delta := \angle(\bar{c}, \bar{n}) \tag{6}$$

with

$$\cos\delta = \frac{\bar{c}\cdot\bar{n}}{|\bar{c}|\cdot|\bar{n}|} = \sin\theta_n \cdot \sin\frac{\theta_n}{2}\cdot\cos(\phi_n - \phi_i) + \cos\theta_n\cdot\cos\frac{\theta_i}{2}. \tag{7}$$
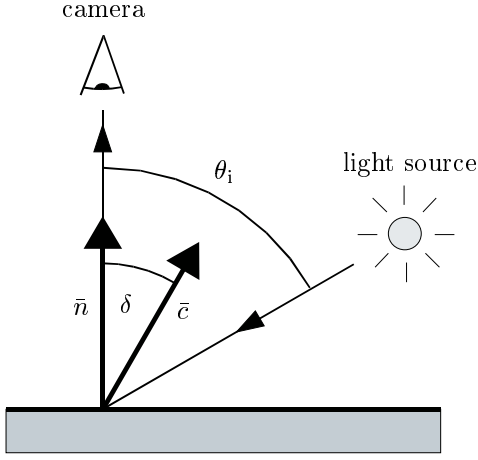
4
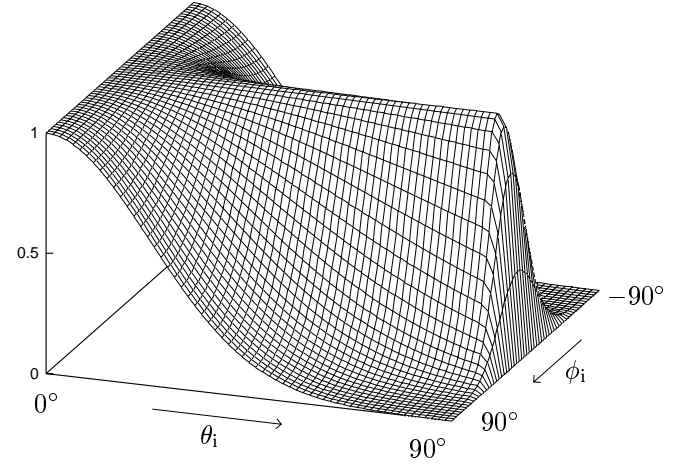
Figure 6. Specular reflection: imaging configuration.

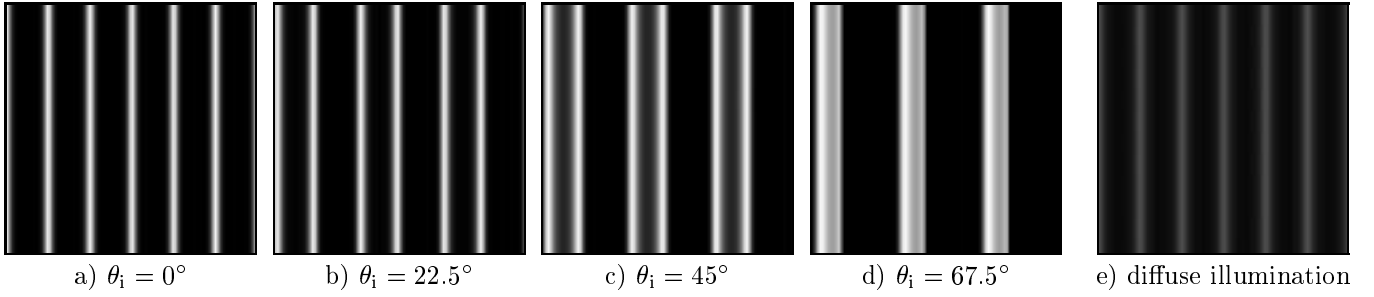**Figure 7.** Image contrast of the specularly reflecting test surface depending on the illumination direction.

a) $\theta_i = 0°$ b) $\theta_i = 22.5°$ c) $\theta_i = 45°$ d) $\theta_i = 67.5°$ e) diffuse illumination

Figure 8. Specularly reflecting test surface: a–d) parallel illumination ($\phi_i = 0$); e) diffuse illumination.

The angles θ_n and ϕ_n are given by:

$$\theta_n \quad = \quad \arccos\left(\frac{1}{\sqrt{1 + A^2 \cdot \sin^2 x}}\right), \tag{8}$$

$$\phi_n \quad = \quad \begin{cases} 0 & \text{for } \sin x \geq 0 \\ \pi & \text{otherwise} \end{cases}. \tag{9}$$

For the following calculations, $\delta = 0.2$ was chosen.

Like Fig. 5, Fig. 8 shows simulated grey-level images of the test surface Fig. (1) illuminated with different light patterns. Images 8a–d were generated by assuming a collimated source for different illumination angles. If we choose a purely diffuse illumination pattern, a much poorer contrast will be obtained (see Fig. 8e). For the calculations the same simplifications as in section 2.3.1 were adopted.

In Fig. 7 the image contrast K according to eq. (4) is plotted depending on the illumination angles θ_i and ϕ_i of a collimated source. The contrast becomes maximal when the illumination direction $\bar{\imath}$ is chosen to be perpendicular to the grooves (here: $\phi_i = 0°$), but in contrast to Fig. 4 the choice of the elevation angle θ_i is practically of no influence for $\phi_i = 0°$. However, this result is due to the fact that the test surface contains patches with many different inclinations. As a general rule, structured surfaces will show a higher dependence on the elevation angle θ_i.[8]

5

2.3.3 Backscatter reflection

As shown in Fig. 2, the backscatter lobe is very similar to the forescatter lobe. It is spread around the direction of the incident light. Although most materials display very little backscatter, it is still perceptible.[14] Since its description can be performed similarly to specular reflection, we will abstain from further considerations. The conclusions drawn in section 2.3.2 can be adopted for this case, if the difference in the reflection direction is taken into account.

2.4 Conclusions

The results of the simulations presented in section 2.3 show that the image contrast, and thus also the signal-to-noise ratio, highly depend on the illumination direction. Furthermore, it is shown that in the case of groove textures a variation of the illumination angle leads to a migration of grey-level patterns through the image. Thus, due to the superposition principle the choice of more homogeneous lighting patterns will generally lead to a contrast attenuation. However, the main problem results from the fact that the selection of an optimal illumination direction depends on the texture, i.e. for inhomogeneously textured surfaces on the spatial coordinates. This means that optimal lighting would imply that different surface areas are illuminated from different directions, which in practice is extremely difficult.

3 IMAGE FUSION

In the second part of the paper, a method is presented that allows to obtain images with optimal lighting even if the surface is not homogeneously textured. As pointed out above, the acquisition of all image areas with maximal contrast requires a spatially varying illumination. The proposed method is based on obtaining a so-called *illumination series*, i.e. a series of images in which each image is acquired using a different illumination direction (θ, ϕ). By means of an appropriate fusion algorithm, an image can be obtained in which every surface area is contained with maximal contrast.

3.1 Acquisition of image series

The images $d(\bar{x}, \bar{\omega})$ of a series are two-dimensional signals with respect to the location $\bar{x} = (x, y)^{\mathrm{T}}$ indexed with the parameter vector describing the acquisition situation $\bar{\omega} = (\phi, \theta)^{\mathrm{T}}$, where $\phi := \phi_i$ and $\theta := \theta_i$ represent azimuth and elevation angle of the illumination direction respectively. Additional parameters, like the integration time of the video camera or the wavelength of the used light, could also be taken into account, if necessary.

An important question deals with the strategy for sampling the illumination space so that (1) image fusion is possible, and (2) the signal of interest is contained in the fusion result. The goal is to obtain all surface areas in good quality with as few images

$$D = \{d(\bar{x}, \bar{\omega}_i), i = 0, \dots, n\} \tag{10}$$

as possible. This problem highly depends on the object geometry as well as on the surface texture and cannot be dealt with in detail here. Some aspects of this problem are discussed in Refs. 9,16.

For illumination series of textured surfaces consisting of a band of straight, parallel grooves, it is not necessary to sample the illumination space two-dimensionally, because such surfaces only show a high contrast if they are illuminated perpendicularly, as shown in section 2.3. Thus, only the elevation angle θ needs to be varied. However, in most cases both illumination angles will have to be varied.

3.2 Fusion approach

The literature on data fusion is extensive, indicating the interest in this topic. However, many of the approaches are *ad hoc*. In this paper, a systematic data fusion approach is used which is based on the minimization of a so-called "energy function"[4]

$$E = E_{\mathrm{D}}(D, r) + \lambda E_{\mathrm{C}}(r), \qquad \lambda > 0. \tag{11}$$

6

$E_{\mathrm{D}}(D, r)$ models the relationship between the given image data (i.e. the image series)

$$D = \{d(\bar{x}, \bar{\omega}_i),\ i = 0, \ldots, n\}, \tag{12}$$

and the fusion result $r(\bar{x})$. $E_{\mathrm{C}}(r)$ models desired characteristics of the fusion result $r(\bar{x})$ or those known a priori. The regularization parameter λ serves to weight both components.

The energy terms $E_{\mathrm{D}}(D, r)$ and $E_{\mathrm{C}}(r)$ are to be defined in such a way that the result is more desirable, the lower the energy is. Consequently, E has to be minimized to obtain $r(\bar{x})$.

By defining Gibb's densities, a connection of this approach with the Bayesian fusion theory and the Markov Random Fields theory can be achieved.[4] Thus, methods for solving inverse problems of statistical mechanics can be also utilized.

3.3 Fusion of 1-D illumination series

For a better understanding, a fusion algorithm for illumination series will be presented first. Following, the fusion task will be generalized in such a way that it will fit within the framework discussed in the last section. It will be shown that the method represents a very efficient approximation for the solution of the fusion problem by energy minimization.

In this section one-dimensional series — i.e. series in which only one parameter is varied — will be treated. An extension to the two-dimensional case will be given in the next section. Fig. 9 shows the structure of the fusion algorithm for the case of a varying azimuth ϕ.
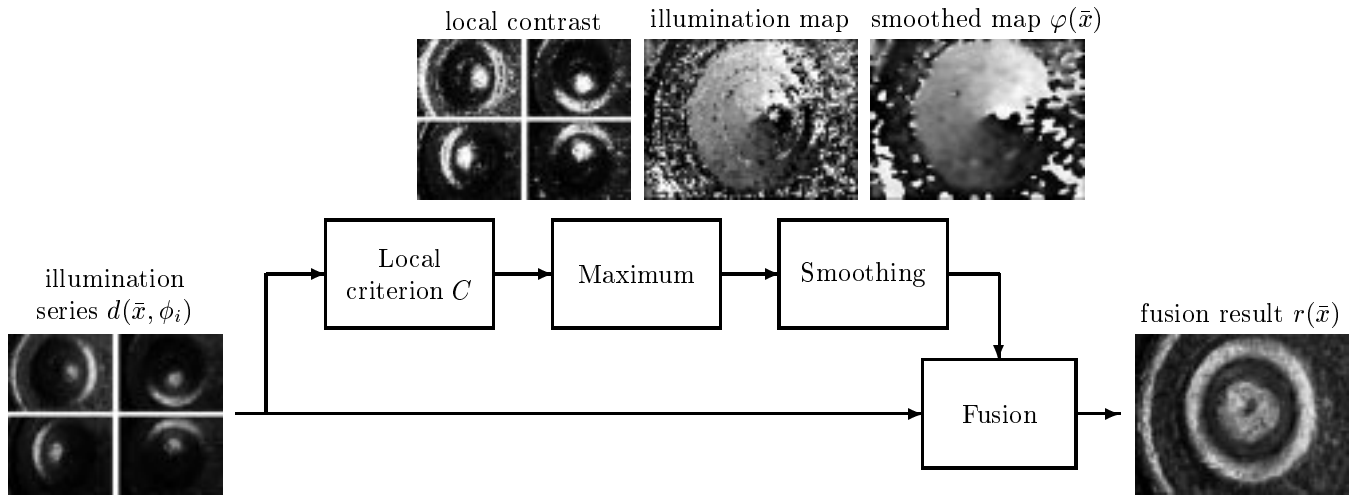

Figure 9. Structure of the algorithm for fusing 1-D illumination series.

The principle of the fusion algorithm consists in the selection of the best illuminated image segments of the series for each location based on a local criterion C. The local grey-level variance and the local entropy are suitable criteria C, if a high-contrast fusion result $r(\bar{x})$ is desired. The selected illumination direction, which is stored for each location $\bar{x}$ in the so-called *illumination map*

$$\tilde{\phi}(\bar{x}) = \arg\max_{\phi_i} C\{d(\bar{x}, \phi_i)\}, \tag{13}$$

has to be a spatial function varying slowly compared to the signal of interest. This is necessary to avoid artifacts in the fusion result. To assure that this condition is satisfied, a smoothing of the illumination map with a binomial low-pass filter is performed:[7]

$$\varphi(\bar{x}) = \angle \mathrm{LP}\{e^{j\tilde{\phi}(\bar{x})}\}. \tag{14}$$

In this step, the cyclicity of ϕ has to be taken into account, because $\phi = \phi + 2\pi k$, $k \in \mathbb{Z}$ holds. Thus, not $\tilde{\phi}(\bar{x})$ itself, but the complex pointer $\exp\left(j\tilde{\phi}(\bar{x})\right)$ has to be smoothed. The resulting function $\varphi(\bar{x})$, which denotes the best-suited local illumination direction, is the angle of the complex result.[11]

The actual fusion is performed by weighted superposition of two adjacent images $d(\bar{x}, \phi_i)$ with a linear interpolator γ taking the best local illumination direction $\varphi(\bar{x})$ into account:

$$r(\bar{x}) = \sum_i d(\bar{x}, \phi_i)\gamma(\varphi(\bar{x}) - \phi_i) = \frac{\varphi(\bar{x}) - \phi_l}{\phi_{l+1} - \phi_l}d(\bar{x}, \phi_l) + \frac{\phi_{l+1} - \varphi(\bar{x})}{\phi_{l+1} - \phi_l}d(\bar{x}, \phi_{l+1}). \tag{15}$$

The interpolation takes care of a smooth transition between ϕ-neighbouring images; see Fig. 10. The narrow extent of γ provides for an averaging of only similarly illuminated images. Thus, an undesirable contrast loss due to destructive interferences of light and shadow in different images of the series is avoided.
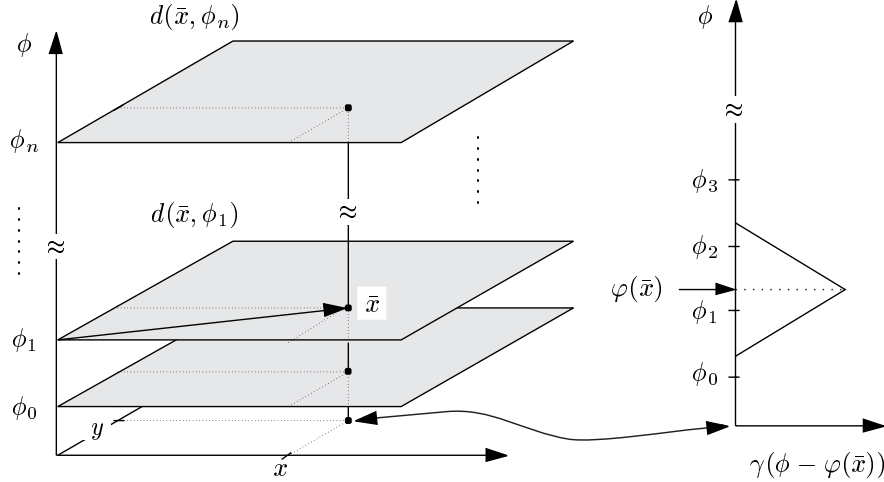

Figure 10. Selection of the best illuminated image segments for fusion.

Three properties of the proposed fusion method are responsible of its good performance:

1. for each location $\bar{x}$, the fusion result $r(\bar{x})$ resembles the best illuminated image $d(\bar{x}, \phi_i)$ of the series;

2. the smoothness of the selected illumination direction $\varphi(\bar{x})$ guarantees that no artifacts are contained in the resulting image $r(\bar{x})$;

3. the resulting image achieves globally good results in the sense of the local measure C.

By formulating energy terms that penalize the non-fulfillment of any of these conditions, an energy function of the form of eq. (11) can be obtained:

$$
\begin{aligned}
E &= \sum_i \sum_{\bar{x}} \left(r(\bar{x}) - d(\bar{x}, \phi_i)\right)^2 \gamma(\phi_i - \varphi(\bar{x})) + \lambda_1 \sum_{\bar{x}} \left(\mathrm{HP}\{\varphi(\bar{x})\}\right)^2 - \lambda_2 \sum_{\bar{x}} C\{r(\bar{x})\} \\
&= E_{\mathrm{D}}(D, r, \varphi) + \lambda_1 E_{\mathrm{S}}(\varphi) + \lambda_2 E_{\mathrm{C}}(r).
\end{aligned}
\tag{16}
$$

This equation represents a compact, implicit formulation of the fusion problem, in which all known and desirable characteristics of the magnitudes involved in the fusion process as well as their mutual relations are given.

The first addend $E_{\mathrm{D}}(D, r, \varphi)$ in eq. (16) provides for data proximity to $r(\bar{x})$. To fulfill the smoothness constraint for the optimal illumination angle $\varphi(\bar{x})$, the second addend $E_{\mathrm{S}}(\varphi)$ penalizes high frequency components of $\varphi(\bar{x})$ by

measuring the energy of the high-pass filtered signal $\mathrm{HP}\{\varphi(\bar{x})\}$. Consequently, this addend represents a smoothness constraint for the optimal illumination angle $\varphi(\bar{x})$. The third addend $E_\mathrm{C}(r)$ checks whether the local criterion C leads to high values in the fusion result $r(\bar{x})$ globally.

If we have a look at the algorithm shown in Fig. 9 again, the analogy between its blocks and the addends of eq. (16) becomes clearer. In both left upper blocks basically $E_\mathrm{C}(r)$ is minimized. The smoothing performed in the right upper block above all provides for a minimization of $E_\mathrm{S}(\varphi)$. Subsequently, the fusion block takes care of a smooth transition between the best images of the series, being equivalent to a minimization of $E_\mathrm{D}(D, r, \varphi)$.

For the assumptions made here, the minimization of E with respect to r and φ would lead to the optimal fusion result at the expense of a very high computation time. The fusion strategy proposed instead, however, represents an *efficient approximation* of the energy minimization approach based on a separate optimization of the addends of eq. (16), and with no need to consider the weighting factors λ_i.

3.4 Fusion of 2-D illumination series

In the more general case of varying the azimuth ϕ as well as the elevation angle θ, the fusion approach given in eq. (16) has to be extended accordingly:

$$E = E_\mathrm{D}(D, r, \varphi, \vartheta) + \lambda_1 E_\mathrm{S}(\varphi) + \lambda_2 E_\mathrm{C}(r) + \lambda_3 E_\mathrm{S}(\vartheta). \tag{17}$$

An additional term proportional to $E_\mathrm{S}(\vartheta)$ provides for smoothness of the locally optimal elevation angle $\vartheta(\bar{x})$. Furthermore, the linear interpolator γ contained in the first term $E_\mathrm{D}(D, r, \varphi, \vartheta)$ has to be expanded to the two-dimensional case. The narrow extent of $\gamma(\varphi, \vartheta, \phi_i, \theta_i)$ only allows images in a neighbourhood around the locally optimal illumination direction $(\varphi(\bar{x}), \vartheta(\bar{x}))$ to contribute to the fusion result $r(\bar{x})$.
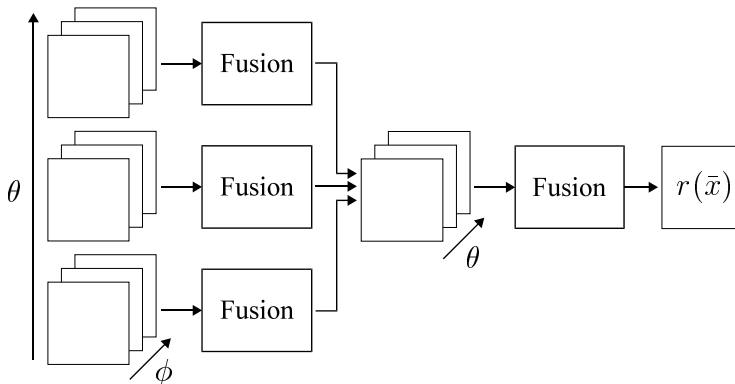

Figure 11. Fusion of 2-D illumination series.

If the illumination space is sampled properly, the fusion task can be treated one-dimensionally, and consequently simplified; see Fig. 11. For certain elevation angles θ_i, $i = 0, \ldots, n$ illumination series are acquired by varying the azimuth ϕ. In the first fusion stage, all image series have to be fused with respect to ϕ. Each of the fusion blocks corresponds to the whole fusion algorithm shown in Fig. 9. The resulting images represent a new image series. By fusing this series with respect to θ, the fusion result $r(\bar{x})$ is obtained.

4   EXPERIMENTAL RESULTS

In this section, experimental results of the fusion methods discussed in section 3 are presented and compared with images which can be obtained without data fusion. To obtain image series, an automated system was set up which consists of a flexible illumination module, and a commercial macroscope. The illumination system is composed of a platform in which 256 LEDs are placed, and a parabolic reflector in the focus of which the object is fixed; see Fig. 12.[10] The location of an LED on the platform determines the direction (θ, ϕ) from which the object surface

is illuminated. By variation of these parameters, any area on the object surface can be acquired with maximum contrast. An opening in the reflector allows image acquisition with a macroscope and a CCD camera. All images throughout this paper were digitized with 512×512 pixels, and 8 bit grey levels.
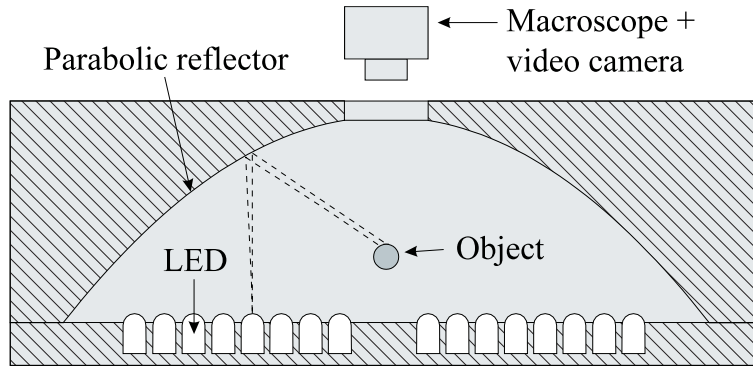

Figure 12. Illumination system.

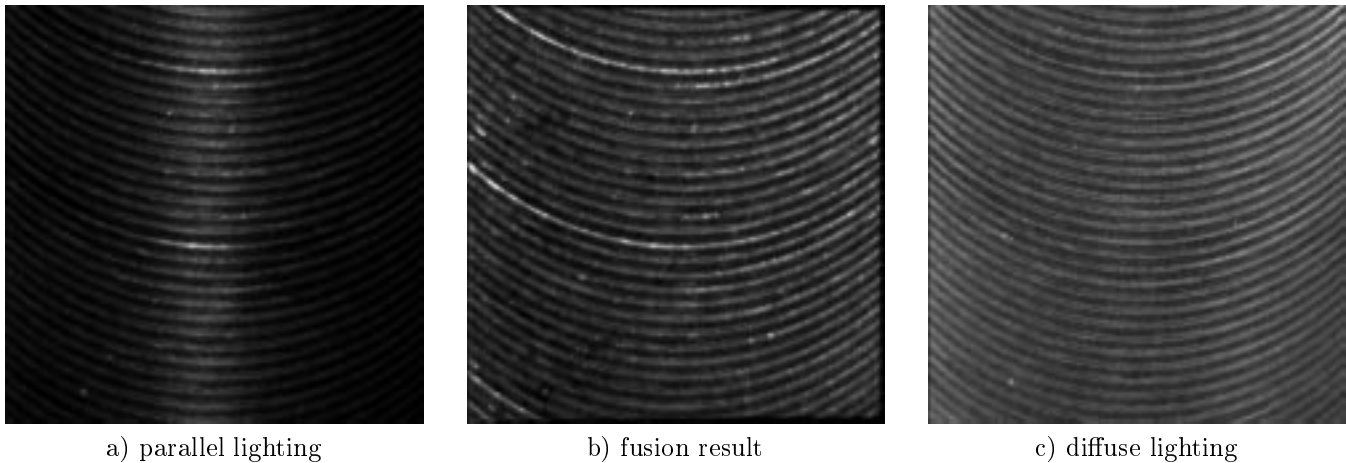a) parallel lighting   b) fusion result   c) diffuse lighting

Figure 13. End-milling surface: a) image no. 8 of the illumination series; b) fusion result (criterion C: variance in a 5×5-mask; smoothing of $\tilde{\phi}(\bar{x})$ with a binomial filter of size 49×49); c) diffuse lighting.

In Fig. 13a, an image of an illumination series consisting of 20 images ($\Delta\phi \approx 5.6°$) of an end-milling texture can be seen. Due to illumination, the texture shows a bright stripe.[3] To fuse the image series, C was chosen as the local grey-level variance in a mask of size 5×5. The illumination map $\tilde{\phi}(\bar{x})$ was smoothed with a circular binomial filter with an impulse response of 49×49 pixels. In the fusion result Fig. 13b, the whole surface is illuminated much better, hitherto hidden details become visible, and the stripe-like inhomogeneity can no longer be recognized. By comparison of the fusion result with the same surface illuminated diffusely (Fig. 13c), it can be stated that in the fusion result the grooves are contained with much higher contrast. Thus, the surface quality can be assessed more accurately.

In Fig. 14a, four images of an illumination series of a firing pin print on a cartridge case are shown. The elevation angle θ was kept constant over the whole series, whereas the azimuth was varied stepwise ($\Delta\phi = 18°$). The fusion result can be seen in Fig. 14b. To fuse the series, the same criterion and the same smoothing filter as in Fig. 13 were chosen in this case. To assess the fusion result, the same object was imaged with diffuse lighting; see Fig. 14c. By comparing both images, it can be noticed that many details in the firing pin print area cannot be seen in the
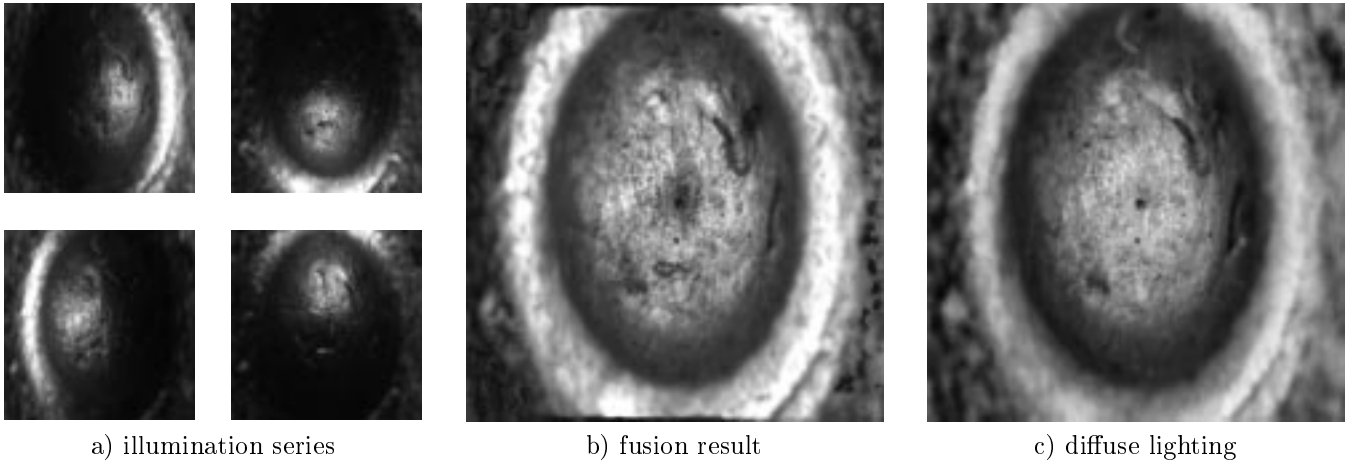
| a) illumination series | b) fusion result | c) diffuse lighting |

Figure 14. Firing pin print: a) illumination series (images nos. 0, 5, 10, and 15); b) fusion result (criterion C: variance in a $5{\times}5$-mask; smoothing of $\tilde{\phi}(\bar{x})$ with a binomial filter of size $49{\times}49$); c) diffuse lighting.

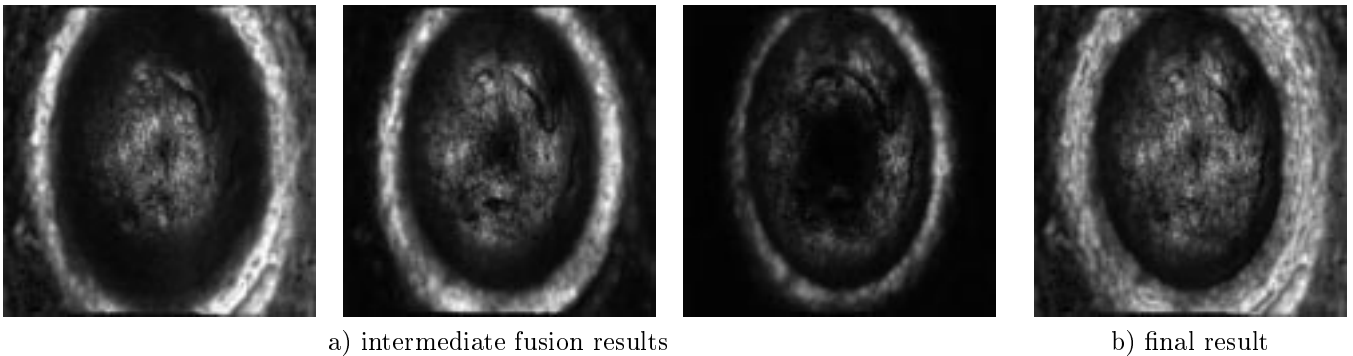| a) intermediate fusion results | b) final result |

Figure 15. Fusion of a 2-D illumination series of a firing pin print: a) intermediate fusion results; b) final fusion result (criterion C: variance in a $5{\times}5$-mask; smoothing of $\tilde{\phi}(\bar{x})$ and $\tilde{\theta}(\bar{x})$ with a binomial filter of size $49{\times}49$).

diffusely illuminated image. Especially, a distinct feature resulting from surface topography (see Figs. 14a and 14b), which represents an important information for forensic examiners, cannot be detected in Fig. 14c. In contrast to this, all details contained in the diffusely illuminated image can also be recognized in the fusion result.

Finally, an example of fusing 2-D illumination series according to section 3.4 will be presented. The illumination series of Fig. 14 is now extended by varying also the elevation angle θ. Fig. 15a shows the results of fusing three 1-D image series of the same firing pin print as in Fig. 14 with respect to ϕ. Within each of the series, the azimuth was varied ($\Delta\phi = 18°$), whereas the elevation angle was kept constant. However, for each series a different elevation angle was chosen. In Fig. 15b the result of fusing all three images with respect to the elevation angle θ is shown. Here, surface features could be obtained with appreciably higher contrast than in the case of 1-D illumination series; see Fig. 14b. Other surfaces were also examined with the proposed method, and similar results could be achieved.

5 SUMMARY

In this paper, methods for obtaining well-illuminated images of surfaces have been presented. To make a decision concerning the choice of a suitable illumination strategy, the image formation process has been discussed, and simulated images of a groove textured surface were analysed. It has been shown that image contrast is highly illumination-dependent, and that the signal of interest contained in a physical texture often would be lost if standard

image acquisition methods were used. To compensate the emerging illumination difficulties, image series were obtained by varying the illumination direction systematically. By means of data fusion, images were combined to an improved result which could not have been acquired physically with only one image. The fusion task has been formulated by means of an energy function. On the one hand its addends describe all known and desirable relations between the image series $\{d(\bar{x}, \omega_i)\}$ and the fusion result $r(\bar{x})$, and on the other hand the known and desirable properties of $r(\bar{x})$ and other relevant magnitudes involved in the fusion process. By minimization of this function, the optimal fusion result with respect to the assumptions met was obtained. In our case, the structure of the energy function allowed to perform the computationally expensive optimization by means of an efficient approximation.

The performance of the proposed algorithms has been demonstrated with images of metallic surfaces. However, the methods presented are also suitable for acquisition of high-quality images of any other object for automated visual inspection purposes. As a rule, surface features could be obtained much more robustly and with higher contrast by means of fusion of illumination series. Hence, the increased effort in image acquisition appears to be absolutely reasonable in many computer vision tasks, where high-quality images are needed.

ACKNOWLEDGEMENTS

REFERENCES

1. J. Beyerer, *Analyse von Riefentexturen*, VDI-Verlag, Düsseldorf, 1994.

2. J. Beyerer and F. Puente León, "Detection of defects in groove textures of honed surfaces", *International Journal of Machine Tools & Manufacture* **37** (3), pp. 371–389, 1997.

3. J. Beyerer and F. Puente León, "Suppression of inhomogeneities in images of textured surfaces", *Optical Engineering* **36** (1), pp. 85–93, 1997.

4. J. J. Clark and A. L. Yuille, *Data Fusion for Sensory Information Processing Systems*, Kluwer, Boston, 1990.

5. M. D'Zmura, "Shading Ambiguity: Reflectance and Illumination", in *Computational Models of Visual Processing*, M. S. Landy and J. A. Movshon, eds., pp. 187–207, MIT Press, Cambridge, 1991.

6. B. K. P. Horn and R. W. Sjoberg, "Calculating the Reflectance Map", *Applied Optics* **18** (11), pp. 1770–1779, 1979.

7. B. Jähne, *Digitale Bildverarbeitung*, Springer, Berlin, 1993.

8. P. Kierkegaard, "Reflection properties of machined metal surfaces", *Optical Engineering* **35** (3), pp. 845–857, 1996.

9. R. Malz, *Codierte Lichtstrukturen für 3-D-Meßtechnik und Inspektion*, Dissertation, Universität Stuttgart, 1992.

10. R. Malz, *Verfahren zum beleuchtungsdynamischen Erkennen und Klassifizieren von Oberflächenmerkmalen und -defekten eines Objektes und Vorrichtung hierzu*. Offenlegungsschrift DE 4123916 A1, Deutsches Patentamt, 1992.

11. K. V. Mardia, *Statistics of Directional Data*, Academic Press, London, 1972.

12. T. S. Newman and A. K. Jain, "A Survey of Automated Visual Inspection", *Computer Vision and Image Understanding* **61** (2), pp. 231–262, 1995.

13. F. Puente León, "Image processing methods for the macroscopic acquisition of high-quality images of surfaces and tools", in *Proc. of the 7th Int. Conf. on Metrology and Properties of Engineering Surfaces*, B.-G. Rosén and R. J. Crafoord, eds., pp. 452–459, Chalmers University of Technology, Göteborg, 1997.

14. H. D. Tagare and R. J. P. deFigueiredo, "A Theory of Photometric Stereo for a Class of Diffuse Non-Lambertian Surfaces", *IEEE Transactions on Pattern Analysis and Machine Intelligence* **13** (2), pp. 133–152, 1991.

15. K. E. Torrance and E. M. Sparrow, "Theory of off-specular reflection from roughened surfaces", *J. Opt. Soc. Amer.* **57** (9), 1105–1114, 1967.

16. S. Yi, R. M. Haralick, and L. G. Shapiro, "Optimal Sensor and Light Source Positioning for Machine Vision", *Computer Vision and Image Understanding* **61** (1), pp. 122–137, 1995.